ARTICLES
https://doi.org/10.1038/s41566-021-00860-5

nature photonics

Ultra-coherent Fano laser based on a bound state in the continuum

Yi Yu[1,2] ✉, Aurimas Sakanas[1,2], Aref Rasoulzadeh Zali[1,2], Elizaveta Semenova[1,2], Kresten Yvind[1,2] and Jesper Mørk[1,2] ✉

It is an important challenge to reduce the power consumption and size of lasers, but progress has been impeded by quantum noise overwhelming the coherent radiation at reduced power levels. Thus, despite considerable progress in microscale and nanoscale lasers, such as photonic crystal lasers, metallic lasers and plasmonic lasers, the coherence length remains very limited. Here we show that a bound state in the continuum based on Fano interference can effectively quench quantum fluctuations. Although fragile in nature, this unusual state redistributes photons such that the effect of spontaneous emission is suppressed. Based on this concept, we experimentally demonstrate a microscopic laser with a linewidth that is more than 20 times smaller than existing microscopic lasers and show that further reduction by several orders of magnitude is feasible. These findings pave the way for numerous applications of microscopic lasers and point to new opportunities beyond photonics.

Since Schawlow and Townes[1], it has been known that the coherence of a laser is limited by quantum fluctuations, with the laser linewidth $\Delta\nu$ scaling inversely with the quality factor (Q-factor), Q, and the laser power, P, $\Delta\nu \propto 1/(PQ^2)$ (refs. [1,2]). The linewidth can be reduced by increasing the power or by increasing Q through enlarging the size of the laser system[3–8] or engineering the spatial profile of the lasing mode[9]. These approaches are exemplified by various macroscopic lasers, where often the linewidth is limited by ambient noise rather than intrinsic quantum noise. As the laser shrinks into the microscopic regime[10–15], quantum fluctuations, and therefore the linewidth, increase substantially due to the reduction of the number of photons in the laser cavity[16]. Realizing ultra-coherent nanoscale lasers is of great importance for numerous applications, such as on-chip communications[17], programmable photonic integrated circuits[18], bio/chemical sensing[19] and quantum and neuromorphic computing[20,21]. An approach to narrowing the linewidth of small lasers is to improve the cavity Q-factor. However, although ultrahigh Q-factors have been attained in passive nanocavities[22], non-radiative cavity loss increases substabtially when active material is introduced to the cavity in order to facilitate stimulated emission (for example, due to free-carrier absorption). Indeed, hardly any improvements in the linewidth of microscopic lasers have been reported during the last decade, and the smallest reported linewidth of nanocavity lasers is still larger than 100 MHz (ref. [23]).

Results

Concept and structure. In this work, we address this long-standing problem by exploring the physics of a bound state in the continuum (BIC)[24], which was demonstrated recently in different physical systems[25–29]. In particular, we consider a bound state formed due to Fano interference[30–32] between the continuum of modes of a terminated waveguide (WG) and the discrete mode of a side-coupled nanocavity (Fig. 1b). At the wavelength of the BIC, the paths of the right-propagating fields through the WG and the nanocavity interfere destructively. If the nanocavity is intrinsically lossless, meaning that its Q-factor is entirely determined by the coupling to the WG, the destructive interference is perfect[33], leading to a Fano mirror with unity reflectivity[33–36]. Therefore, a BIC is formed and is localized in the nanocavity and a virtual cavity region (Fano cavity) between the left termination of the WG and the right Fano mirror. In reality, unless the structure is of infinite extent, the nanocavity loss is always finite, turning the BIC into a quasi-BIC[37] (Fano BIC). The BIC nature of the Fano mode can be identified by a sensitive dependence of the Q-factor on the structural parameters[37], as illustrated by the red curve in Fig. 1c. Only at a specific value of the cavity length can the standing wave condition be fulfilled while, simultaneously, the Fano mirror reflectivity achieves its maximum (Supplementary Note A.2). In comparison, ordinary lasers can adjust their wavelength in order to fulfil the phase-matching condition, and the Q-factor changes only slowly with laser parameters, as illustrated by the black curve in Fig. 1c. Although a resonance-based BIC is fragile in nature, the Fano interference enhances its robustness by introducing a large phase variation (π) of the reflected field from the Fano mirror across the nanocavity resonance[36]. This helps to minimize the detuning $\delta_0 = \omega_0 - \omega_s$ between the nanocavity resonance ω_0 and the laser frequency ω_s upon perturbations, as exemplified by the variation of δ_0 around its zero (symmetry) point as the cavity length changes (Fig. 1c). Therefore, the laser frequency partially tracks the Fano mirror reflection maximum (BIC wavelength). At the BIC wavelength, the Fano mode exhibits a highly non-uniform light distribution, with the optical intensity being much higher in the discrete mode region of the nanocavity than in the continuum region of the WG. This is in contrast to an ordinary cavity mode, whose intensity distribution is rather uniform across the entire cavity region (Fig. 1a). The spatial asymmetry of the Fano BIC can be harnessed by incorporating active material only in the continuum region while leaving the discrete mode region passive. Photons generated by stimulated emission in the active region thus get stored predominantly in the passive region, which features much smaller loss and smaller fluctuations of the refractive index than the active region. Therefore, compared to ordinary cavity modes, the composite Q-factor of the Fano BIC can be significantly increased.

The general property of the Fano BIC at the heart of the linewidth reduction is the strong frequency dependence of the optical

---

[1]DTU Fotonik, Technical University of Denmark, Lyngby, Denmark. [2]NanoPhoton – Center for Nanophotonics, Technical University of Denmark, Lyngby, Denmark. ✉e-mail: yiyu@fotonik.dtu.dk; jesm@fotonik.dtu.dk

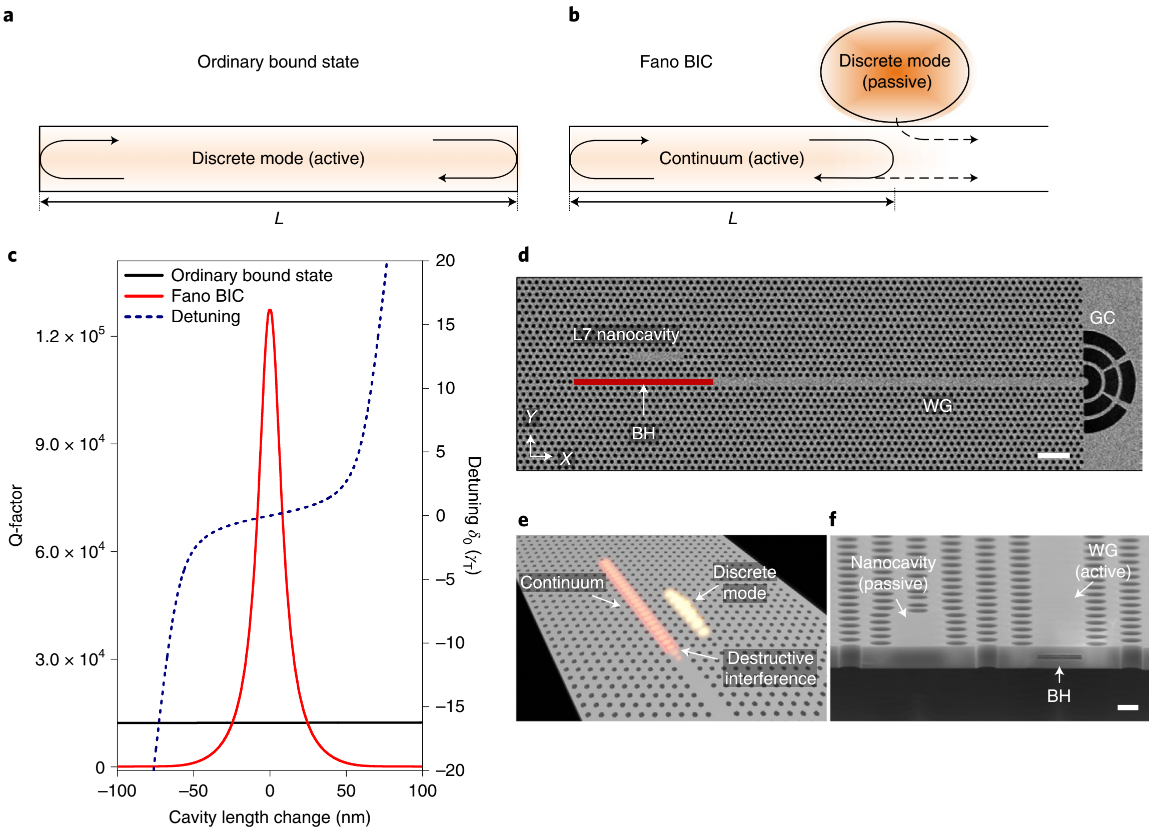

Fig. 1 | Concept of BIC laser based on Fano resonance. a, Ordinary bound state in conventional Fabry–Pérot lasers. Photons are generated and confined in the active region. **b**, Optical BIC formed in the Fano laser. Photons are generated in the active region, which has a continuum of modes, but are predominantly stored in the low-loss passive region. **c**, Example of calculated variation of Q-factor versus cavity length L for the Fano BIC laser (solid red line) and a conventional Fabry–Pérot laser (solid black line). The Fano BIC laser has an intrinsic Q-factor Q_v of 5.0×10^5 and a coupling Q-factor Q_c of 3.0×10^3 for its discrete mode, while the Fabry–Pérot laser has an intrinsic Q-factor Q_m due to mirror loss of 5.0×10^5. Both lasers have a cavity length L of 5 µm, a loss rate γ_i due to active material of $3.8\times10^{10}\,\mathrm{s}^{-1}$, and a cavity round trip time $1/\gamma_{in}$ of 0.54 ps. The blue dashed line depicts the calculated variation of the detuning $\delta_0=\omega_0-\omega_s$ of the Fano BIC laser frequency, ω_s, from the nanocavity resonance, ω_0. **d**, Scanning electron microscope (SEM) image of a fabricated Fano BIC laser based on an InP photonic crystal (PhC) membrane structure with a buried heterostructure (BH, red rectangle) gain region and a grating coupler (GC) at the end of the WG. Scale bar, 2 µm. **e**, Schematic of the optical Fano BIC. **f**, SEM image of the cross-section of a fabricated Fano BIC laser showing the active WG containing a BH and the passive nanocavity. The BH is etched away after the device cleaving. Scale bar, 200 nm.

phase across the resonance. This implies a long dwell time in the discrete low-loss region of the structure, which provides storage of photons that counteracts phase diffusion induced by spontaneous emission quantum noise in the active region. Quantitatively, we may account for this by calculating the Q-factor of the Fano BIC, taking into account the spatial distribution of the state. Assuming that the left mirror is lossless and the laser works at the symmetry point ($\omega_s=\omega_0$), the right Fano mirror reflectivity can be expressed as $|r_{R,FL}|=\gamma_c/\gamma_T$ where γ_v, γ_c and $\gamma_T=\gamma_v+\gamma_c\,(\gamma_v\ll\gamma_c)$ are the nanocavity intrinsic loss rate, coupling (between the nanocavity and the WG) loss rate and total loss rate, respectively, which relate to the nanocavity intrinsic and coupling Q-factors as $Q_v=\omega_0/(2\gamma_v)$ and $Q_c=\omega_0/(2\gamma_c)$ (Supplementary Note A.1). The Q-factor of the Fano BIC then becomes (Supplementary Note A.2)

$$Q=\frac{\omega_0}{2}\frac{\gamma_{\rm in}+\gamma_{\rm c}}{\gamma_{\rm in}\gamma_{\rm v}+\gamma_{\rm c}\gamma_{\rm i}},\qquad(1)$$

where γ_{in} and γ_i are the inverse round trip time and the loss rate due to active material in the Fano cavity. Since the ratio of photons stored in the discrete mode region relative to the continuum region of the Fano BIC is given by γ_{in}/γ_c (Supplementary Note A.2), we can design a Fano BIC such that the major proportion of the photons is localized in the low-loss passive region by ensuring $\gamma_{in}\gg\gamma_c$. This is in contrast to coupled-cavity lasers, where the lasing mode cannot be concentrated in the passive region, neither in the parity-time-symmetric nor in the parity-time-broken regime[38]. It shows that if one wants to achieve the same Q-factor as that of the Fano BIC (equation (1)) using an ordinary bound state in a conventional laser, the loss rate due to the active material needs to be smaller than the intrinsic loss rate of the nanocavity (that is, $\gamma_i<\gamma_v$) (Supplementary Note A.2). This is not the case even in high-quality active devices, meaning that it is impossible for a conventional Fabry–Pérot laser to achieve the same Q-factor as the Fano BIC laser. Compared to a Fabry–Pérot laser with a passive cavity Q-factor identical to the intrinsic Q-factor of the nanocavity, the effective Q-factor of the Fano BIC laser is approximately $1+\gamma_{in}/\gamma_T$ times higher (Supplementary Note A.2). This enables the achievement of narrower linewidth in Fano BIC lasers.

Using a Langevin approach to include quantum noise, we derive the following approximate expression for the linewidth of the Fano BIC laser above threshold (Supplementary Note A.3)

$$\Delta\nu_{\rm FL}=\frac{1}{2\pi}\frac{1+\alpha^2}{\left(1+\gamma_{\rm in}/\gamma_{\rm T}\right)^2}\frac{G_{\rm s,FL}n_{\rm sp}}{2I_{\rm FL}}.\qquad(2)$$

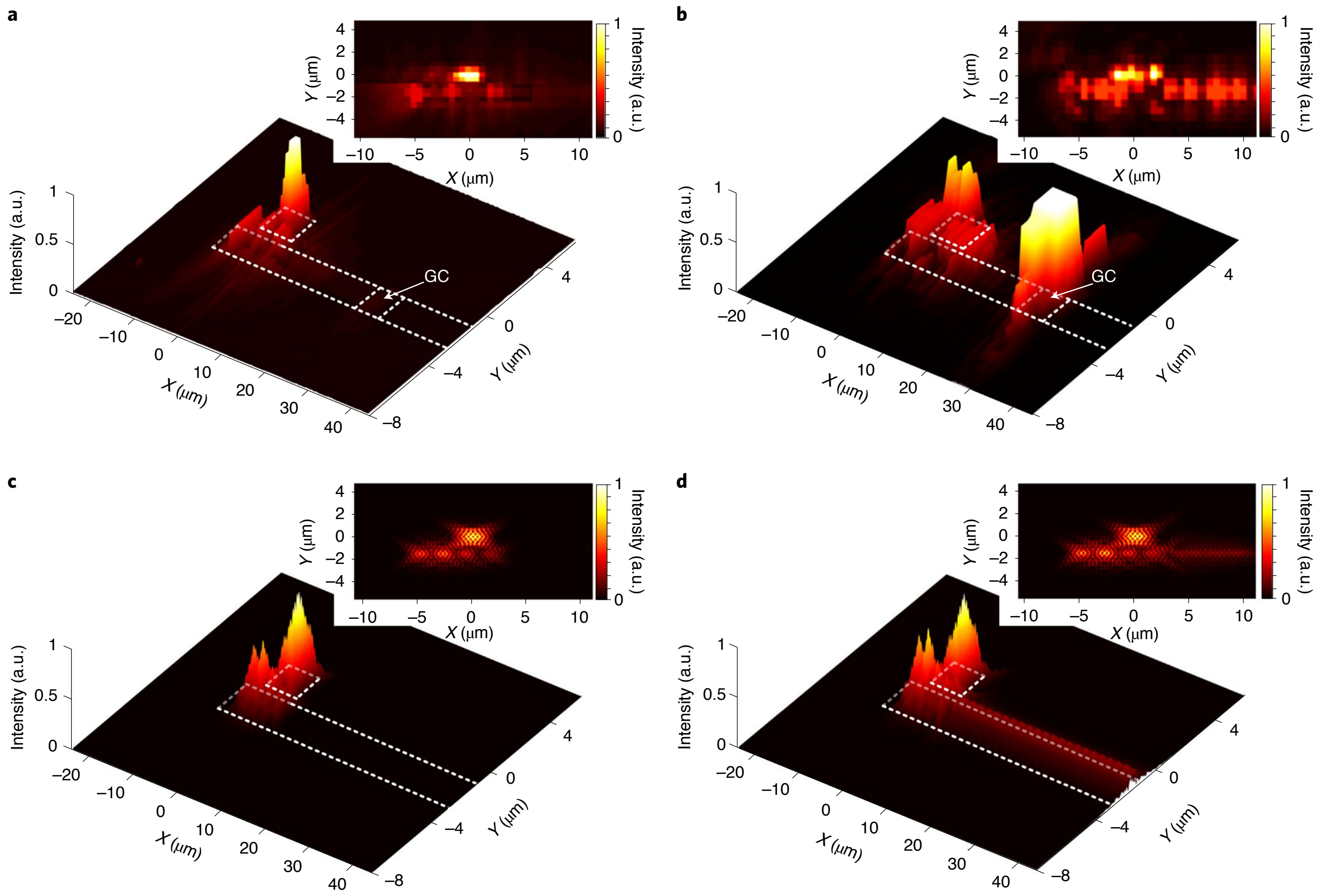

Fig. 2 | Mode patterns of Fano BIC laser. a,**b**, Infrared images of the lasing patterns of fabricated Fano BIC lasers, where the lasing wavelength coincides with (**a**) or is detuned from (**b**) the peak of the Fano mirror. The insets are top views of the emission profiles. The white-dashed square at the left shows the position of the nanocavity, the white-dashed square on the right indicates the grating coupler (GC), and the white-dashed long rectangle indicates the semi-open WG. **c**,**d**, Corresponding calculated electric field profiles ($|E|$) of the Fano BIC mode at the central plane of the PhC membrane, with the lasing wavelength being on-resonance (**c**) and off-resonance (**d**) with respect to the BIC wavelength. The insets are top views of the electric mode profiles.

Here, α is the usual linewidth enhancement factor[2], $G_{\mathrm{s,FL}}$ is the threshold modal gain, n_{sp} is the population inversion factor and I_{FL} is the number of photons in the Fano cavity, which depends on the pump power. From our theory, we find that it is possible to decrease the linewidth of a microcavity laser by more than three orders of magnitude by using a Fano BIC mode (Supplementary Note A.3). In equation (2), this effect is seen by the proportionality of the linewidth to γ_{T}^2. For lasers working away from the symmetry point, the quantum noise may instead increase for decreasing γ_{T} (Supplementary Note A.3). In contrast to the approach of spatial mode profile engineering to reduce the linewidth[9], the optical confinement factor is fixed for the Fano BIC laser, and the reduction of the linewidth therefore does not compromise the laser threshold (Supplementary Note A.2). External cavity lasers are a well-known and commercially important approach to reducing laser linewidth. However, such devices are macroscopic in nature, as well as suffering from multimode effects that require external filtering and careful alignment[4–8]. The Fano BIC laser does not have these trade-offs and, as we have shown, can be scaled into the microscopic regime.

We base our experimental demonstration on semiconductor InP PhC membrane structures on a silicon platform (Fig. 1d–f). Here, the continuum of modes is provided by a PhC line-defect WG, terminated at the left end by a conventional PhC mirror formed by air holes. The discrete mode is the fundamental mode of an L7 nanocavity created by omitting seven air holes (Fig. 1e), and its interaction with the continuum of modes constitutes the right Fano mirror. In particular, whereas previous experimental demonstrations of Fano structures had active material incorporated into the entire membrane[36], it is key for the BIC concept proposed here to localize the gain in the continuum region only. To achieve this, we use semiconductor BH technology[11]. The BH contains a single InGaAsP/InAlGaAs quantum well and is localized in the continuum region (Fig. 1f). Process optimization[39] has enabled excellent lateral alignment even at the nanoscale. The laser is equipped with a broadband grating coupler[40] at the end of the WG to facilitate optical pumping. Details of the structure design and fabrication process can be found in Supplementary Notes B and C.1.

Mode pattern and lasing characteristics. The Fano BIC laser is first characterized by vertical pumping with a continuous-wave light source at 1,480 nm through the grating coupler (Fig. 1d), and the emission is detected vertically above the nanocavity (Supplementary Notes B and C.2). The infrared image of the lasing pattern (Fig. 2a) clearly shows an optical Fano BIC with the expected characteristics as the oscillation condition is fulfilled. This is verified by comparison to the electric field profile obtained by finite-difference time-domain simulations (Fig. 2c). The field profile is shown in the centre of the membrane but changes little when considering planes

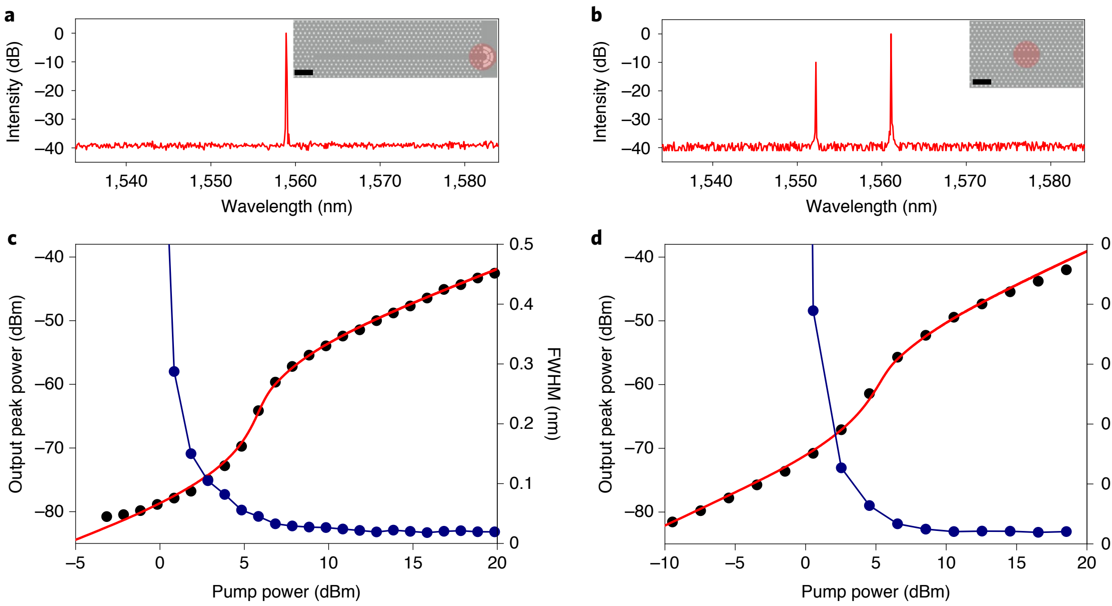

Fig. 3 | Lasing characteristics of Fano BIC laser. a, Measured (normalized) emission spectra above threshold of the Fano BIC laser. Inset: the Fano BIC laser is optically pumped through the grating coupler. Scale bar, 1.7 μm. **b**, Measured emission spectra above threshold of an equivalent Fabry–Pérot laser, realized as a conventional PhC line-defect laser. Inset: the Fabry–Pérot laser is optically pumped directly into the nanocavity. Scale bar, 1.7 μm. **c**,**d**, Output peak power (black dots and red lines) and full-width at half-maximum (FWHM, blue dots and lines) of the lasing spectra versus pump power for the Fano BIC laser (**c**) and the Fabry–Pérot laser (**d**). The black dots are experimental data, and the red lines are theoretical fits.

at or above the membrane surface. In particular, the mode intensity is much stronger in the discrete region than in the continuum region of the WG. This is in accordance with the small calculated optical mode volume V_m of 0.26 μm^3. In contrast, the light pattern in a laser where the BIC condition is not fulfilled has a larger proportion of the mode residing in the active region, and light spills out through the grating coupler (Fig. 2b). This is also in good agreement with simulations (Fig. 2d), where a structure with an effective Fano cavity length ~10 nm off the peak is considered (Supplementary Note C.4). These results illustrate the characteristic sensitive properties of a resonance-based BIC.

Next, we measure the lasing characteristics of the Fano BIC laser. For comparison, we also show results for a conventional PhC line-defect (L7) laser, which is identical to the discrete region of the Fano BIC laser, except that the BH is now embedded in the line-defect cavity. The L7 laser can be treated as an effective Fabry–Pérot laser[40–42]. As shown in Fig. 3a, the optical spectrum of the Fano BIC laser exhibits a single lasing peak at ~1,560 nm, which agrees with the fundamental mode of the equivalent Fabry–Pérot laser, where, however, two longitudinal modes are present (Fig. 3b). This demonstrates the good mode selection property of the Fano BIC laser enabled by the narrowband Fano mirror[36]. The measurements can be fitted with a rate equation model (Supplementary Note A.1) and show clear transitions to lasing at pump thresholds of 5.45 dBm (3.8 dBm) for the Fano (Fabry–Pérot) laser (Fig. 3c,d). A notable difference from an all-active Fano laser[36] is the suppression of self-pulsations, which can be traced back to the absence of active material in the nanocavity. The laser linewidth (Fig. 3c,d), obtained as the full-width at half-maximum of the optical spectra, decreases with pump power and quickly goes below the resolution of our optical spectrum analyser (0.02 nm). Around the threshold, where the active material is close to transparency, the linewidth is narrower for the Fano BIC laser than the Fabry–Pérot laser, indicating a larger Q-factor. Considering the nature of the Fano BIC, it might be expected that the laser be very sensitive towards ambient changes, in particular the temperature. However, due to the good thermal conductivity of InP as well as the near-identical scaling of phase changes in the continuum region and the resonance frequency shift of the discrete region, the laser is actually quite robust (Supplementary Note C.4). This makes the Fano BIC laser a good candidate for sensing applications that require the device to be resistant to uncontrolled environmental perturbations.

Linewidth characterization. In order to measure the laser linewidth below the resolution limit of the optical spectrum analyser, we apply a self-homodyne technique, where the laser light interferes with a delayed version of itself[43]. In order to reduce the impact of $1/f$ noise[44] and other slowly varying ambient noise sources, we use a 200 m fibre delay line, which is still one order of magnitude longer than the laser coherence length (Supplementary Note C.2). The measured photocurrent spectra of both lasers exhibit Lorentzian lines (Fig. 4a,b) and are well fitted by our theoretical model (Supplementary Note C.2). The linewidths narrow as the pump power increases, which is in accordance with the Schawlow–Townes linewidth formula. The measurements using a longer delay line of 10 km show slightly broader linewidths (for example, the smallest linewidth of the Fano and Fabry–Pérot laser increases by a factor of ~1.10) (Supplementary Note C.2). Results for two batches (1 and 2) of nominally identical devices fabricated from the same wafer but with separate lithography and processing steps are shown. The main difference between the batches is an improved bonding quality in batch 2.

The measured variation of the linewidth with pump power is well explained by our theory (see equation (2)). Compared to the conventional linewidth formula, the linewidth of the Fano BIC laser is reduced by a factor $\chi=(1+\gamma_\mathrm{in}/\gamma_\mathrm{T})^2$, indicating that the higher the nanocavity Q-factor is, the narrower the Fano BIC laser linewidth becomes. By using the values of $\gamma_\mathrm{in}=1.9\times10^{12}\,\mathrm{s}^{-1}$ and $\gamma_\mathrm{T}=7.5\times10^{11}\,\mathrm{s}^{-1}$, as estimated from the numerical simulations, one gets $\chi=12.5$, which matches well with the experimental results, which are 220 MHz / 15.5 MHz = 14 at 11.5 times the threshold for batch 1 and 92 MHz / 5.8 MHz = 15.9 at 27.5 times the threshold

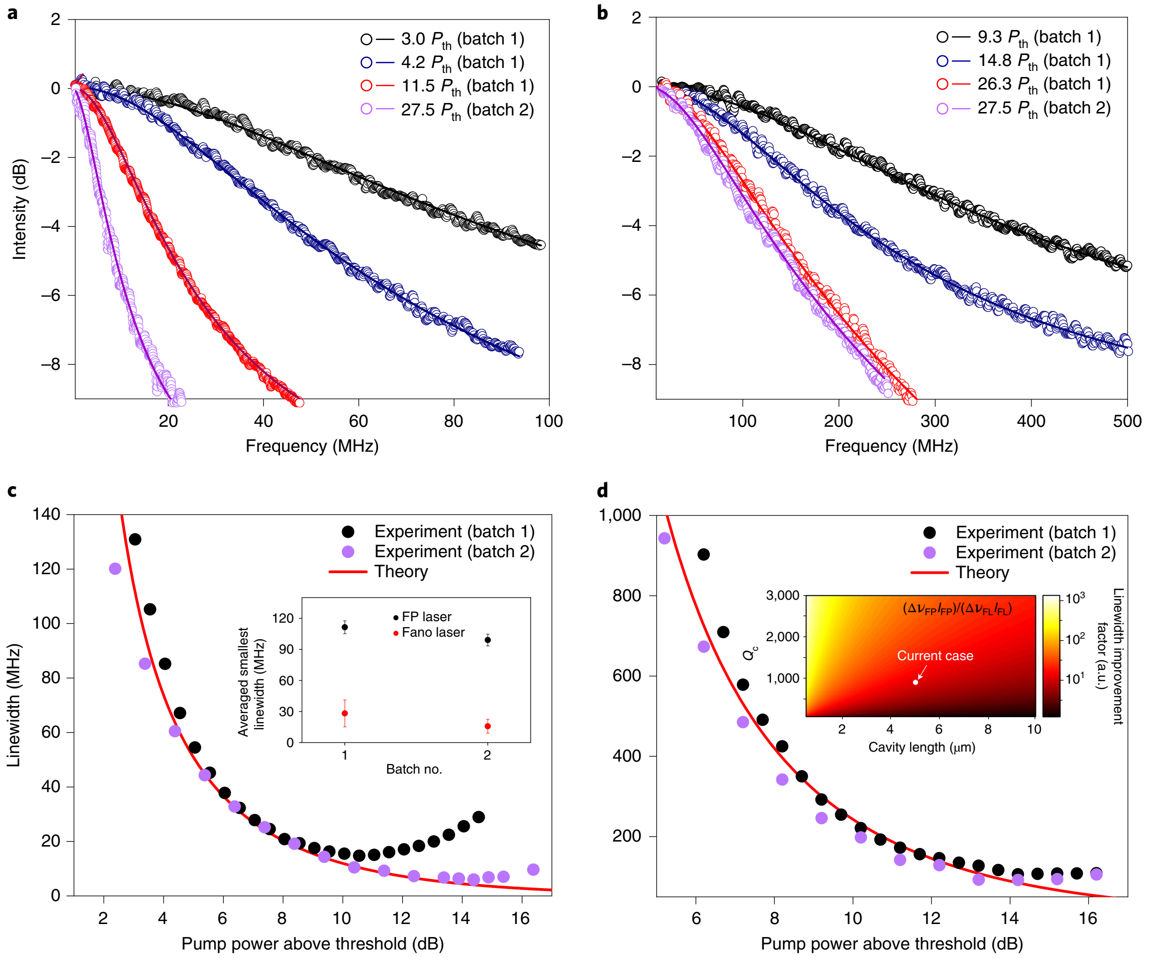

Fig. 4 | Laser linewidth measurements. a,**b**, Measured self-homodyne frequency spectra of the Fano BIC laser (**a**) and the Fabry–Pérot laser (**b**). The pump power levels for the Fano BIC laser are 3.0 (black), 4.2 (blue) and 11.5 (red) times the threshold pump power P_{th} for batch 1, and 27.5 (purple) times P_{th} for batch 2. The pump power levels for the Fabry–Pérot laser are 9.3 (black), 14.8 (blue) and 26.3 (red) times the threshold pump power P_{th} for batch 1, and 27.5 (purple) times P_{th} for batch 2. The markers are experimental results, and the solid lines are theoretical fits. **c**,**d**, Extracted laser linewidths of the Fano BIC laser (**c**) and the Fabry–Pérot laser (**d**) versus pump power. The pump power has been normalized, with 0 dB corresponding to the threshold pump power. The black and purple dots are experimental results, and the solid red lines are theoretical calculations. The inset in **c** shows the mean and standard deviation (error bars) of the smallest linewidths of five nominally identical Fano BIC lasers (red dots) and five nominally identical Fabry–Pérot lasers (black dots) of batches 1 and 2. The inset in **d** shows the linewidth improvement factor as a function of the nanocavity coupling Q-factor Q_c and the Fano cavity length. The nanocavity intrinsic Q-factor is fixed at $Q_v = 1.3\times10^5$. The white dot indicates our current operation point.

for batch 2 (Fig. 4c,d) (Supplementary Note A.3). For high pump powers, the linewidth first saturates and then increases. This saturation and re-broadening is a general phenomenon seen for many lasers[23,45] and may be ascribed to thermal effects, $1/f$ noise, optical nonlinearities and mechanical vibrations (Supplementary Note C.2). The larger re-broadening seen for the Fano BIC laser may be due to the phase-matching condition, which is absent for the Fabry–Pérot laser. The later onset of linewidth re-broadening seen for batch 2 is ascribed to improved thermal conductivity due to the higher bonding quality. As shown in the inset of Fig. 4c, we fabricated and measured five nominally identical Fano BIC lasers for each batch, and their smallest linewidths all lie within the range of 14–45 MHz (5.8–22 MHz) for batch 1 (batch 2), in contrast to the Fabry–Pérot lasers, where the smallest linewidths are in the range of 106–115 MHz (92–105 MHz) for batch 1 (batch 2). In all cases, the spectral coherence for Fano BIC lasers is thus much improved compared to the equivalent Fabry–Pérot lasers (Supplementary Notes C.3 and C.4). An improved tolerance towards fabrication disorder for the Fano BIC laser can be achieved by increasing the coupling coefficient γ_c between the discrete and the continuum region. Besides, fabrication inaccuracies can be compensated for by index tuning by, for example, placing microheaters near the laser cavity to tune the nanocavity resonance or the phase delay in the WG[46].

Discussion

In addition to the linewidth itself, the linewidth–output power product is also an important metric, which is equivalent to the linewidth–photon number product $\Delta\nu_{FL}I_{FL}$ (Supplementary Note A.3). As seen from equation (2), $\Delta\nu_{FL}I_{FL}$ is proportional to $G_{s,FL}/\chi$, in which $G_{s,FL}$ is dominated by the propagation loss of the active material, except for short Fano cavities or large Q_c, where the mirror loss becomes important. The inset in Fig. 4d shows how the improvement factor $\mu = G_{s,FP}\chi / G_{s,FL}$ depends on Q_c and L. $G_{s,FP}$ is the threshold modal gain of the equivalent Fabry–Pérot structure, with the power reflectivity of the laser mirror kept constant at 99.74%. Our current case corresponds to an improvement by one order of magnitude (see the white dot in the inset of Fig. 4d), since a relatively low Q_c and large L were chosen to relax fabrication constraints. However, as L decreases and Q_c increases, the improvement factor can reach 10^3, corresponding to a linewidth reduction of two orders of magnitude (Supplementary Note A.3). This implies that as laser sizes shrink even further into the nanoscale (that is, γ_{in} increases), the Fano BIC laser geometry becomes increasingly advantageous. Even higher improvement factors are possible but require a larger Q_c and thus a larger Q_v of the discrete region in order to maintain a low laser threshold. This may be achieved by optimizing the fabrication processes or adopting a hybrid approach, where a low-loss material is employed for the discrete region[8]. Another very interesting but experimentally challenging possibility is to replace the (left) broadband mirror with a second Fano resonance. Such an approach was used by Sato et al.[47] to dynamically control the Q-factor.

We have proposed and demonstrated a new approach for reducing the linewidth of a laser. It relies on combining the concepts of a BIC and a Fano resonance and allows reducing the linewidth of microscopic laser by several orders of magnitude. Experimentally, we demonstrated a linewidth down to 5.8 MHz, which is more than 20 times smaller than previously reported for microscopic lasers[23,45,48]. With this, our laser meets the requirements for 40 Gbits coherent communication[49]. Furthermore, our laser concept can be used to realize integrated sensors[50], with the demonstrated linewidths allowing identification of protein/DNA with concentrations on the order of attomolar, which is difficult to attain using other proposed nano-sensors[51]. Our findings are based on the Fano–Feshbach type resonance[31] and are general for the class of Fabry–Pérot type BIC, which allows many different realizations[25], including the use of heterogeneous[8] or hybrid[52] integration as well as structures with smaller footprint[13,53].

Online content

Any methods, additional references, Nature Research reporting summaries, source data, extended data, supplementary information, acknowledgements, peer review information; details of author contributions and competing interests; and statements of data and code availability are available at https://doi.org/10.1038/s41566-021-00860-5.

Received: 24 November 2020; Accepted: 12 July 2021;
Published online: 12 August 2021

References

1. Schawlow, A. L. & Townes, C. H. Infrared and optical masers. *Phys. Rev.* **112**, 1940 (1985).
2. Henry, C. Theory of the linewidth of semiconductor lasers. *IEEE J. Quantum Electron.* **18**, 259–264 (1982).
3. Young, B. C., Cruz, F. C., Itano, W. M. & Bergquist, J. C. Visible lasers with subhertz linewidths. *Phys. Rev. Lett.* **82**, 3799–3802 (1999).
4. Mørk, J., Tromborg, B. & Mark, J. Chaos in semiconductor lasers with optical feedback: theory and experiment. *IEEE J. Quantum Electron.* **28**, 93–108 (1992).
5. Tager, A. A. & Petermann, K. High-frequency oscillations and self-mode locking in short external-cavity laser diodes. *IEEE J. Quantum Electron.* **30**, 1553–1561 (1994).
6. Liang, W. et al. Ultralow noise miniature external cavity semiconductor laser. *Nat. Commun.* **6**, 7371 (2015).
7. Stern, B., Ji, X., Dutt, A. & Lipson, M. Compact narrow-linewidth integrated laser based on a low-loss silicon nitride ring resonator. *Opt. Lett.* **42**, 4541–4544 (2017).
8. Tran, M. A., Huang, D. & Bowers, J. E. Tutorial on narrow linewidth tunable semiconductor lasers using Si/III-V heterogeneous integration. *APL Photon.* **4**, 111101 (2019).
9. Santis, C. T., Vilenchik, Y., Satyan, N., Rakuljic, G. & Yariv, A. Quantum control of phase fluctuations in semiconductor lasers. *Proc. Natl Acad. Sci. USA* **115**, E7896–E7904 (2018).
10. Painter, O. et al. Two-dimensional photonic band-gap defect mode laser. *Science* **284**, 1819–1821 (1999).
11. Matsuo, S. et al. High-speed ultracompact buried heterostructure photonic-crystal laser with 13 fJ of energy consumed per bit transmitted. *Nat. Photon.* **4**, 648–654 (2010).
12. Wu, S. et al. Monolayer semiconductor nanocavity lasers with ultralow thresholds. *Nature* **520**, 69–72 (2015).
13. Crosnier, G. et al. Hybrid indium phosphide-on-silicon nanolaser diode. *Nat. Photon.* **11**, 297–300 (2017).
14. Khajavikhan, M. et al. Thresholdless nanoscale coaxial lasers. *Nature* **482**, 204–207 (2012).
15. Oulton, R. F. et al. Plasmon lasers at deep subwavelength scale. *Nature* **461**, 629–632 (2009).
16. Bjork, G., Karlsson, A. & Yamamoto, Y. On the linewidth of microcavity lasers. *Appl. Phys. Lett.* **60**, 304 (1992).
17. Sun, C. et al. Single-chip microprocessor that communicates directly using light. *Nature* **528**, 534–538 (2015).
18. Bogaerts, W. et al. Programmable photonic circuits. *Nature* **586**, 207–216 (2020).
19. Ge, C. et al. External cavity laser biosensor. *Lab Chip* **13**, 1247–1256 (2013).
20. Carolan, J. et al. Universal linear optics. *Science* **349**, 711–716 (2015).
21. Shen, Y. et al. Deep learning with coherent nanophotonic circuits. *Nat. Photon.* **11**, 441–446 (2017).
22. Song, B.-S., Noda, S., Asano, T. & Akahane, Y. Ultra-high-Q photonic double-heterostructure nanocavity. *Nat. Mater.* **4**, 207–210 (2005).
23. Kim, J. et al. Narrow linewidth operation of buried-heterostructure photonic crystal nanolaser. *Opt. Express* **20**, 11643–11651 (2012).
24. von Neumann, J. & Wigner, E. Über merkwürdige diskrete Eigenwerte. *Phys. Z.* **30**, 465–467 (1929).
25. Hsu, C. W., Zhen, B., Stone, A. D., Joannopoulos, J. D. & Soljačić, M. Bound states in the continuum. *Nat. Rev. Mater.* **1**, 16048 (2016).
26. Plotnik, Y. et al. Experimental observation of optical bound states in the continuum. *Phys. Rev. Lett.* **107**, 183901 (2011).
27. Molina, M. I., Miroshnichenko, A. E. & Kivshar, Y. S. Surface bound states in the continuum. *Phys. Rev. Lett.* **108**, 070401 (2012).
28. Kodigala, A. et al. Lasing action from photonic bound states in continuum. *Nature* **541**, 196–199 (2017).
29. Ha, S. T. et al. Directional lasing in resonant semiconductor nanoantenna arrays. *Nat. Nanotechnol.* **13**, 1042–1047 (2018).
30. Fano, U. Effects of configuration interaction on intensities and phase shifts. *Phys. Rev.* **124**, 1866–1878 (1961).
31. Miroshnichenko, A. E., Flach, S. & Kivshar, Y. S. Fano resonances in nanoscale structures. *Rev. Mod. Phys.* **82**, 2257 (2010).
32. Limonov, M. F., Rybin, M. V., Poddubny, A. N. & Kivshar, Y. S. Fano resonances in photonics. *Nat. Photon.* **11**, 543–554 (2017).
33. Suh, W., Wang, Z. & Fan, S. Temporal coupled-mode theory and the presence of non-orthogonal modes in lossless multimode cavities. *IEEE J. Quantum Electron.* **40**, 1511–1518 (2004).
34. Tanaka, Y. et al. Dynamic control of the Q factor in a photonic crystal nanocavity. *Nat. Mater.* **6**, 862–865 (2007).
35. Mørk, J., Chen, Y. & Heuck, M. Photonic crystal Fano laser: terahertz modulation and ultrashort pulse generation. *Phys. Rev. Lett.* **113**, 163901 (2014).
36. Yu, Y., Xue, W., Semenova, E., Yvind, K. & Mørk, J. Demonstration of a self-pulsing photonic crystal Fano laser. *Nat. Photon.* **11**, 81–84 (2017).
37. Rybin, M. & Kivshar, Y. Supercavity lasing. *Nature* **541**, 164–165 (2017).
38. Hodaei, H. et al. Parity-time-symmetric microring lasers. *Science* **346**, 975–978 (2014).
39. Sakanas, A., Semenova, E., Ottaviano, L., Mørk, J. & Yvind, K. Comparison of processing-induced deformations of InP bonded to Si determined by e-beam metrology: direct vs. adhesive bonding. *Microelectron. Eng.* **214**, 93–99 (2019).
40. Tsai, C.-C., Mower, J. & Englund, D. Directional free-space coupling from photonic crystal waveguides. *Opt. Express* **19**, 20586 (2011).
41. Lalanne, P., Sauvan, C. & Hugonin, J. P. Photon confinement in photonic crystal nanocavities. *Laser Photon. Rev.* **2**, 514–526 (2008).
42. Xue, W. et al. Threshold characteristics of slow-light photonic crystal lasers. *Phys. Rev. Lett.* **116**, 063901 (2016).
43. Okoshi, T., Kikuchi, K. & Nakayama, A. Novel method for high resolution measurement of laser output spectrum. *Electron. Lett.* **16**, 630–631 (1980).
44. Mercer, L. B. 1/*f* frequency noise effects on self-heterodyne linewidth measurements. *J. Lightwave Technol.* **9**, 485–493 (1991).
45. Bagheri, M. et al. Linewidth and modulation response of two-dimensional microcavity photonic crystal lattice defect lasers. *IEEE Photon. Technol. Lett.* **18**, 1161–1163 (2006).
46. Konoike, R. et al. On-demand transfer of trapped photons on a chip. *Sci. Adv.* **2**, e1501690 (2016).
47. Sato, Y. et al. Strong coupling between distant photonic nanocavities and its dynamic control. *Nat. Photon.* **6**, 56–61 (2012).
48. Piels, M. et al. Laser rate equation-based filtering for carrier recovery in characterization and communication. *J. Lightwave Technol.* **33**, 3271–3279 (2015).
49. Seimetz, M. Laser linewidth limitations for optical systems with high-order modulation employing feed forward digital carrier phase estimation. In *Proc. Optical Fiber Communication Conference/National Fiber Optic Engineers Conference* OTuM2 (Optical Society of America, 2008).

50. Lončar, M., Scherer, A. & Qiu, Y. Photonic crystal laser sources for chemical detection. *Appl. Phys. Lett.* **82**, 4648–4650 (2003).
51. Watanabe, T. et al. Ion-sensitive photonic-crystal nanolaser sensors. *Opt. Express* **25**, 24469 (2017).
52. Birowosuto, M. D. et al. Movable high-Q nanoresonators realized by semiconductor nanowires on a Si photonic crystal platform. *Nat. Mater.* **13**, 279–285 (2014).
53. Lu, F. et al. Nanopillar quantum well lasers directly grown on silicon and emitting at silicon-transparent wavelengths. *Optica* **4**, 717–723 (2017).

Publisher's note Springer Nature remains neutral with regard to jurisdictional claims in published maps and institutional affiliations.

© The Author(s), under exclusive licence to Springer Nature Limited 2021, corrected publication 2021

Methods

Theoretical model of the Fano BIC laser. The model of the Fano BIC laser is established by combining coupled mode equations with conventional rate equations[36]. The coherence properties of the Fano BIC laser are analysed using the Langevin approach to include quantum noise in the model. More details are provided in Supplementary Note A.

Design and fabrication of the PhC BH Fano BIC laser. Three-dimensional finite-difference time-domain simulations are used for the design. We consider a PhC structure having a lattice constant $a = 428$ nm and hole radius $R = 89$ nm and focus on the L7-type nanocavity created by omitting seven air holes in an array. First, through shifting several holes around the nanocavity, we achieve a vertical (intrinsic) Q-factor Q_v of $\sim 1.44 \times 10^5$ for the fundamental mode of the L7 nanocavity at a wavelength close to the gain peak of the quantum well. Next, we side-couple the optimized L7 nanocavity to a standard W1-type open WG. The width of the WG containing the BH is adjusted to control the cavity-WG coupling to realize a coupling Q-factor Q_c of 810. After that, we block the left part of the WG with air holes, leading to the broadband left mirror. Twelve holes are omitted in the WG between the left mirror and the centre of the nanocavity to fulfil the phase-matching condition around the nanocavity resonance peak, thereby forming the Fano cavity. Subsequently, the three outermost air holes at the left mirror are slightly shifted to fine-tune the round trip phase of the light in the WG as well as to minimize the light scattering loss at the left mirror, in order to obtain near-perfect destructive interference for transmission to the WG through-port. More details are provided in Supplementary Note B.

The BH PhC samples are fabricated on a heterogeneously integrated InP-on-Si wafer. First of all, an InP wafer containing a single InGaAsP quantum well and an InGaAs sacrificial layer is directly bonded to a Si substrate, with thermally grown oxide serving as a sacrificial layer for the final device membranization. Then the InP substrate and InGaAs sacrificial layers are removed by wet etching, and the device processing starts by defining the BH mask pattern by e-beam lithography using HSQ resist. After exposure, the wafer is dry etched, leaving the quantum well material only in mesa structures under the HSQ mask and a remaining thin InP layer. InP is then selectively regrown, essentially encapsulating the quantum well regions. After the HSQ mask removal, the second regrowth planarizes the sample. Subsequently, a 200 nm SiN hard-mask layer is deposited, the ZEP resist is spin-coated and another e-beam is used for aligning and exposing PhC patterns onto the prefabricated BH regions. These patterns are then transferred to the device layer by a two-step dry etching process, where SiN is first etched away in the ZEP mask openings, and then, after ZEP removal, InP is dry etched. The final air-suspended InP membrane is realized by dipping the sample in BHF solution, which removes the thermal glass underneath the PhC cavity structures as well as the remaining SiN mask from the top. More details are provided in Supplementary Note C.1.

Experimental setup and laser linewidth measurements. The laser samples are vertically pumped with a 1,480 nm laser diode using a micro-photoluminescence setup, with precise control of pump intensity, pump position and pump area and monitored by an infrared camera. The full-width at half-maximum of the pump spot is fixed at ~3 µm by an objective lens. The emission from the PhC sample is collected vertically using the same objective lens with a numerical aperture of 0.65. The transmission efficiency from the pump diode to the objective is ~30%, and the pumping efficiency is ~10 dB higher for the Fano BIC laser through the grating coupler than through the Fano cavity. This pumping efficiency is similar to that of an equivalent Fabry–Pérot laser (PhC L7 laser), which has a higher-order mode close to 1,480 nm that facilitates absorption of the pump light. The vertical collection efficiency is ~27% for collecting light above the nanocavity and ~70% for collecting light above the grating coupler. All measurements are performed with continuous-wave injection at room temperature. After being isolated from the reflected pump beam by a long-pass filter, the output signal is characterized using an optical spectrum analyser.

To measure the laser linewidth, the collected output laser field is first passed through an optical isolator and then amplified using a low-power erbium-doped fibre amplifier cascaded with a tunable optical band-pass filter to suppress the noise floor. After the filter, the signal passes through a self-homodyne interferometer setup before being detected by a photodiode and monitored with a radio frequency spectrum. More details are provided in Supplementary Note C.2.

Data availability

All data in this study are available within the paper and its Supplementary Information. Further source data will be made available on reasonable request.

Code availability

The code used for modelling the data is available from Y.Y. on reasonable request.

Acknowledgements

We thank K. S. Mathiesen for assistance with sample fabrication and characterization and M. Xiong for inductively coupled plasma etching optimization and assistance with sample characterization. This work was supported by the Danish National Research Foundation through NanoPhoton – Center for Nanophotonics (grant no. DNRF147), the European Research Council (ERC) under the European Union Horizon 2020 Research and Innovation Programme (grant no. 834410 Fano) and Villum Fonden though the NATEC Center (grant no. 8692).

Author contributions

Y.Y., A.R.Z. and J.M. developed the theory. Y.Y. established the importance of the quality factor of the Fano BIC mode. Y.Y. and A.R.Z. performed the phase noise simulations. Y.Y. designed the Fano BIC laser. A.S., E.S. and K.Y. developed the BH nanofabrication technology. A.S. fabricated the devices with the assistance of Y.Y., Y.Y. performed the measurements with the assistance of A.S., and Y.Y. analysed the results. J.M. initiated and supervised the project. J.M. and Y.Y. planned the research. Y.Y. and J.M. wrote the manuscript. All authors commented on the manuscript.

Competing interests

The authors declare no competing interests.

Additional information

Supplementary information The online version contains supplementary material available at https://doi.org/10.1038/s41566-021-00860-5.

Correspondence and requests for materials should be addressed to Y.Y. or J.M.

Peer review information *Nature Photonics* thanks Yeshaiahu Fainman, Andrey Miroshnichenko and Fabrice Raineri for their contribution to the peer review of this work.

Reprints and permissions information is available at www.nature.com/reprints.